Fall December 30, 2020

A Hole Transport Bilayer for Efficient and Stable Inverted Perov-skite Solar Cells

Dhandapani Venkataraman

A Hole Transport Bilayer for Efficient and Stable Inverted Perovskite Solar Cells

Hamza Javaid,† Volodimyr V. Duzhko, *,‡ and D. Venkataraman*, †

† Department of Chemistry, University of Massachusetts Amherst, Amherst, Massachusetts 01003-9303, United States

‡ Department of Polymer Science and Engineering, University of Massachusetts Amherst, Amherst, Massachusetts 01003-9303, United States

KEYWORDS: hole transport bilayers, energy levels, efficiency and stability, inverted p-i-n structures, perovskite solar cells

ABSTRACT We demonstrate that a PTAA/CuI bilayer as a hole transport layer (bilayer HTL) leads to efficient and stable inverted, i.e., p-i-n, perovskite solar cells (PSCs). We observed that devices with a single PTAA interlayer have an average power conversion efficiency (PCE) of 18.1%. In contrast, devices with a bilayer show an enhanced average PCE of 19.4%, with a maximum PCE of 20.34%. The XRD and AFM studies show an improved crystallinity and larger grain size of perovskite films on the CuI surface. Data from ultraviolet photoelectron spectroscopy and impedance spectroscopy suggest that devices with bilayer HTL have increased built-in potential within the device with an enhanced upward band bending at the CuI interface. Compared to devices with a single CuI interlayer, the presence of PTAA in the bilayer-based devices leads to significant suppression of current hysteresis and stable current output at the maximum power point. The bilayer-based devices demonstrate remarkable long-term stability in an inert atmosphere.

1. Introduction

The photovoltaic community is excited about metal halide perovskites because their optoelectronic properties and solution-based fabrication methods are most suited to realize efficient thin-film solar cells at low manufacturing cost. After the first reports of perovskite solar cells (PSC),[1–3] power conversion efficiencies (PCEs) of PSCs have steadily increased from ~3% to ~25% in single-junction devices in a short time.[4] Development of fabrication methods,[5,6] compositional engineering,[7] passivations of surface defects,[8] engineering of advanced device structures [9,10] have been among the significant steps in improving the PCE towards the theoretical Shockley-Queisser limit of 33%,[11] and in prolonging the long-term stability of PSCs.

State-of-the-art PSCs with record PCEs have a regular n-i-p architecture.[12–14] PSCs with the inverted p-i-n architecture have lower PCEs, [17,18] but they have key features that are attractive from a large-scale manufacturing point-of-view. We can fabricate p-i-n devices without multiple high-temperature processing steps.[15,16] Therefore, we can use flexible substrates or incorporate tandem architectures via layer-by-layer fabrication. The lower PCE's in p-i-n devices has been attributed primarily to defects in these devices that assist recombination. Thus, the research in this area is focused on passivating these defects using organic ligands.

An alternate approach would be to use hole transport layers that enable nucleation and growth of perovskite films with lower defect density to minimize charge recombination and have optimum frontier orbital energy levels to maximize charge extraction. In early p-i-n PSCs, poly(3,4-ethylenedioxythiophene) polystyrene-sulfonate (PEDOT:PSS) was used as the HTL.[21,22] Huang and co-workers demonstrated that devices with poly[(bis(4-phenyl)(2,4,6-trimethylphenyl)amine] (PTAA) as HTL performed better and attributed the improved performance to an improved morphology of perovskite films and favorable energy levels that reduce the bulk and interfacial charge recombination.[23] Yet, studies also show that a large density of deep trap states is located at the PTAA/perovskite interface, limiting the efficiency of solar cells.[24] Cuprous iodide (CuI) is another HTL that has been used as top HTL in n-i-p devices and as bottom HTL in p-i-n devices.[25,26] CuI is inexpensive, solution processible, has high electrical conductivity, and good chemical stability making it suitable for PSCs. As a wide-band gap semiconductor, CuI possesses good optical transparency and potentially suitable energy levels for charge/exciton blocking.[26] However, devices with CuI as an HTL have not been demonstrated to have high efficiency and long-term stability.

We reasoned that if we use multi-layer HTLs instead of a single HTL, we can take advantage of the constituent layers' complementary properties.[28] Many electron transport layers (ETL) in the state-of-the-art devices are composed of two or more layers.[27] Multi-layer charge transport layers allow us to choose HTL pairs with appropriate work functions that set up an energy level cascade and appropriate surface energy to nucleate perovskite layer. Multiple layers can also help passivate surface defects, block charge extraction at wrong electrodes, and create physical barriers for ionic and moisture diffusion.[29–33] Herein, we report highly efficient and stable p-i-n perovskite solar cells with a bilayer HTL using PTAA and CuI. We show that bilayer devices outperform devices with single HTLs of PTAA, CuI, or PEDOT:PSS HTLs. Using X-ray diffraction (XRD) and atomic force microscopy (AFM), we show that perovskite films on CuI surface have higher crystallinity and larger grain size in both the single-layer CuI- and bilayer PTAA/CuI-based HTL devices. The ultraviolet photoelectron spectroscopy (UPS) and impedance spectroscopy (IS) with Mott-Schottky analysis indicate an increased built-in potential in the device and an enhanced upward band bending in the perovskite film at the interface with CuI. They originate from the higher work function of CuI. Overall, these properties are expected to increase the PCE of devices, particularly open-circuit voltage (*Voc)* and fill factor

(*FF*), in agreement with our experimental observations. Additionally, We observed that the hysteresis in current density (*J*)-voltage (*V*) curves in devices with single CuI HTL is significantly suppressed in bilayer HTL-based devices. We speculate that iodide migration, mainly from CuI top layer, into PTAA bottom layer leads to removal of the hysteresis in device operation, to the enhancement of p-type doping of CuI, and to p-type doping of PTAA. Hence, a high PCE and long-term stability originate from each component's properties in the bilayer HTL and a synergistic effect of their interaction.

2. Experimental Section

Materials. The ITO-coated glass substrates (15 ohms sq^{-1}) were obtained from Kintec Company. PEDOT:PSS solution (AI 4083) was purchased from Ossila. Methylammonium iodide (MAI) and formamidinium iodide (FAI) were purchased from Dyesol. PTAA, CuI, and PbI, phenyl-C_{61}-butyric acid methyl ester ($PC_{61}BM$), as well as anhydrous toluene, acetonitrile, gamma-butyrolactone (GBL), chlorobenzene, 2,2,2-trifluoroethanol (TFE), dimethyl sulfoxide (DMSO) were purchased from Sigma-Aldrich. All materials were used without further purification.

Device fabrication. ITO-coated glass substrates were cleaned by ultrasonic treatment in detergent, water, acetone, and isopropyl alcohol for 10 min each. HTL solutions were prepared by dissolving PTAA in toluene (1.5 mg ml^{-1}) and CuI in acetonitrile (15 mg/ml). The as-prepared PTAA and CuI solutions were then spin coated atop of ITO-coated glass substrates at 3500 rpm for 40 s and 3000 rpm for 60 s, respectively. PTAA and CuI samples were annealed at 100 °C for 10 mins, while PEDOT:PSS was annealed at 150 °C for 30 mins. In the post-annealing step, PTAA HTL was treated with ozone for 40 s. For PTAA/CuI bilayer, CuI was spin coated atop of ozone-treated PTAA at 3500 rpm and subsequently annealed at 100 °C for 10 min. A 1.4 M precursor solution of MAI/FAI (0.95:0.05) and PbI_2 (1:1) in GBL/DMSO (v/v 7:3) was prepared and stirred overnight at 60 °C. The perovskite solution was then spin coated on the HTL by a two-step spin-coating procedure: 1500 rpm for 20 s and 2000 rpm for 60 s. During the second step, chlorobenzene (antisolvent) was dripped onto the substrate after 20 s. As-cast films were left at 65 °C for 1 min, followed by thermal annealing at 100 °C for 10 min inside the N_2-filled glovebox (<1 ppm of O_2, <1 ppm of H_2O). A solution of $PC_{61}BM$ (15 mg ml^{-1}) in chlorobenzene was spin coated atop the perovskite layer at 1000 rpm for 60 s. Then, C_{60}-N in TFE (3 mg ml^{-1}) was spin coated at 4000 rpm to give a 15 nm-thick film. Finally, 100 nm Ag metal (area 5.2 mm^2) was thermally deposited onto the active layer under a high vacuum (2 x 10^{-6} mbar).

Device characterization. The *J-V* studies were performed under AM1.5G (100 mW cm^{-2}) irradiation using Newport SOL2A 300 W solar simulator. For each configuration, 4 substrates were fabricated in total in 3 different batches. The devices were kept under illumination for 2 minutes, and multiple *J-V* scans were obtained from -0.2 to 1.2 V (forward bias) or 1.2 V to -0.2 V (reverse bias) at a scan rate of 0.14 V s^{-1}. The *J-V* curve was recorded after the J_{SC} was stabilized. The light intensity was adjusted using NREL-calibrated Si solar cell with a KG-5 filter. The average device metrics were calculated based on 7 devices for PTAA, CuI and PEDOT:PSS, and 8 devices for PTAA/CuI HTLs. Agilent 4294A Precision Impedance Analyzer was used for impedance spectroscopy. A 50 mV AC amplitude and 100 kHz frequency were used for *C-V* measurements for Mott-Schottky analysis. All *J-V* and *C-V* measurements were performed inside the N_2-filled glovebox.

The samples for AFM measurement were prepared by spin coating the HTLs and perovskite solution on glass substrates using the same device fabrication procedure given above. AFM measurements were made in air using an Asylum Research MFP3D stand-alone AFM. The probes (ANSCM-PT) used were Pt/Ir-coated (≈25 nm) Si probes with a spring constant of 1–5 N m^{-1} as supplied from AppNano. Scans were typically 5 μm × 5 μm at a scan speed of 1.0 Hz. The grain size distribution was extracted using ImageJ software.

Powder X-ray diffraction (PXRD) measurements were taken from 2θ = 10° to 50° under Cu Kα (1.542 Å) with a PANalytical X'Pert3 X-ray diffractometer.

All samples were fabricated identical to the respective steps in the solar cell fabrication procedure for UPS measurements. The measurements were performed with Electron Spectroscopy for Chemical Analysis instrument (Scienta Omicron Nanotechnology, model ESCA+S) at a base pressure of 4×10^{-10} mbar. The instrument configuration consisted of a He discharge lamp (He I line, 21.2 eV) as the UV excitation source and a hemispherical SPHERA energy analyzer. A sample bias of -3 V was used to collect the low kinetic energy electrons. The binding energy scale, which is given with reference to the instrument Fermi level, was shifted accordingly. The E_{SEC} were determined from the intersection of a tangent line to the signal onset with the abscissa axis; the respective vacuum levels were taken 21.2 eV away from E_{SEC}. The HOMO/VB energies were determined from the intersection of lines tangent to the signal onsets and low-binding energy background. The instrument resolution of ~0.1 eV was calculated from the full width at half maximum of a Fermi level of Ar+-sputtered silver.

Photoluminescence studies were carried out emission studies were carried out on an Agilent Cary Eclipse Fluorescence spectrometer. Films were excited at 475 nm, and the emission spectra were measured in the range of 700 – 820 nm. The absorption studies were carried out on an Agilent Cary 50 Bio UV-Visible Spectrometer.

3. Results and Discussion

Inverted PSCs with p-i-n device architecture consisting of ITO/HTL/$FA_{0.05}MA_{0.95}PbI_3$/[6,6]-phenyl C_{61} butyric acid methyl ester ($PC_{61}BM$)/C_{60}-N/Ag were fabricated using four different HTLs. A C_{60}-N (Figure S1) was used as an interfacial modification layer at the Ag electrode.[20] **Figure 1**a shows the photocurrent density-voltage (*J-V*) curves measured in the reverse scan direction for the devices with PEDOT:PSS, PTAA, CuI, or PTAA/CuI as HTLs. Figure 1b shows the *J-V* curves for the device with bilayer PTAA/CuI HTL for both scan directions. Figure 1c-f summarizes the average short-circuit current density (J_{SC}), fill factor (*FF*), $V_{OC,}$ and efficiency (η) values. Table S1 lists the average and best device performance metrics. The operation of PEDOT:PSS-based devices with an average PCE of 13.2 ± 0.63% is consistent with many other studies.[23,26,27] Replacement of PEDOT:PSS with PTAA leads to a significant enhancement of average PCE up to 18.1 ± 0.76% (Figure 1c). In particular, the J_{SC} and V_{OC} of these PTAA-HTL

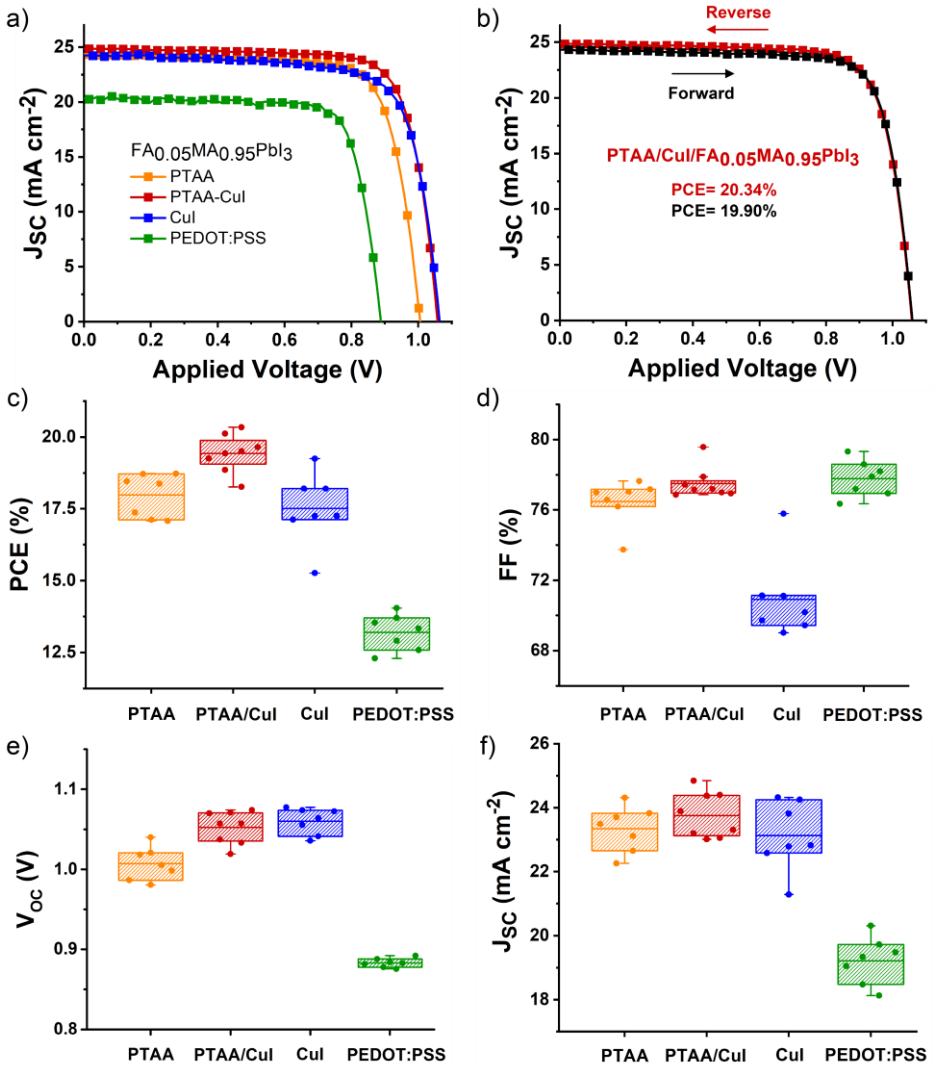

Figure 1. (a) The reverse scan J-V curves for different HTL-containing $FA_{0.05}MA_{0.95}PbI_3$ devices; (b) The forward and reverse scan J-V curves for PTAA/CuI bilayer containing device and (c-f) the average device performance characteristics for PTAA, PTAA/CuI, CuI and PEDOT:PSS-based $FA_{0.05}MA_{0.95}PbI_3$ devices.

devices increased dramatically. Despite the highest V_{OC} of ~1.06 V and large J_{SC} of 23.1 mA cm^{-2} in CuI-HTL devices, their average PCE is comparable to PTAA devices due to a lower *FF* of 71.4 ± 2.1%. Low *FF* in CuI-HTL devices could be due to low shunt resistance (avg. ~16.9 kΩ) compared to the PTAA-based devices (avg. ~38 kΩ). Low shunt resistance indicates the presence of small pinholes in the CuI film that could form during the nucleation due to random crystal orientation. The presence of pinholes could cause leakage at the interface for hole collection, thus can contribute to the observed low *FF*. Note also that, while small current hysteresis was observed for PEDOT:PSS-based devices, the performance of CuI-HTL devices strongly depends on the scan direction (Figure S2 and Table S2). When we introduced a PTAA layer between CuI and ITO, the device performance significantly improved. The average *FF* increased to 77.5 ± 0.8% the devices maintained a high average J_{SC} and V_{OC} of 23.8 mA cm^{-2} and 1.05 V, respectively. The devices with bilayer PTAA/CuI achieve the best average PCEs of 19.4 ± 0.66% with a fairly narrow distribution of all device metrics. The best device produced a PCE of 20.34% (Table S2). Figure S3 shows the external quantum efficiency (EQE) profile of multiple bilayer devices, where broad photoresponses with high values were obtained.

Iodide vacancies in CuI have been reported to form trap states above the valence band.[34,35] During forward and reverse voltage sweeps, these trap states can be reversibly populated and depopulated with iodide ions or holes at the timescale of scan rates. We observed that the hysteresis is dramatically suppressed in bilayer PTAA/CuI-based devices (Figure 1b). The hysteresis in bilayer PTAA/CuI-based devices is comparable to the PTAA-based devices (Figure S2a and S2d). On the other hand, significantly smaller hysteresis in PEDOT:PSS-based devices indicate that the perovskite active layer is not the primary origin for this effect. Therefore, we speculate that diffusion of excess iodide ions from CuI leads to the doping of PTAA,[36] which improves the hole conductivity of both layers and optimizes the energy level alignment, enabling a highly efficient device with negligible hysteresis. The doping of conjugated polymers by iodide ions is well known.[37,38]

In a p-i-n device architecture, the HTL influences the perovskite films' morphology and crystallinity. Therefore, to understand the improvement in device performance in bilayer HLT containing devices, we imaged the morphology and grain size

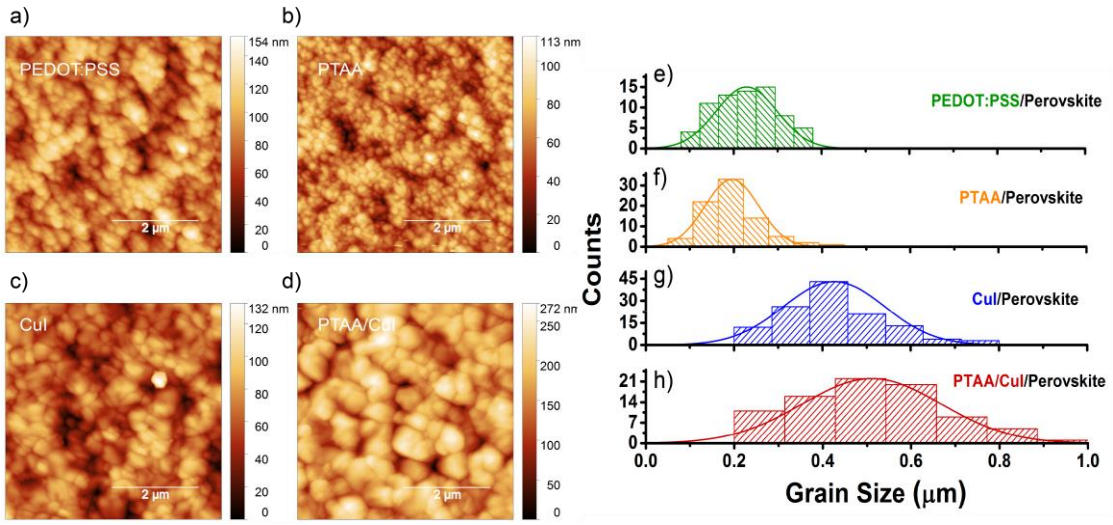

Figure 2. (a-d) Atomic force microscopy (AFM) images and (e-h) respective grain size distribution for $FA_{0.05}MA_{0.95}PbI_3$ films spin-coated on (a,e) PEDOT:PSS (b,f) PTAA (c,g) CuI and (d,h) PTAA/CuI HTL coated glass substrates.

of the as-prepared perovskite films on different HTLs using atomic force microscopy (AFM). The images showed uniform coverage of the perovskite films for all HTLs, ensuring fewer pinholes and hence, better charge transport in the solar cell devices (**Figure 2**a-d). The nucleation and growth processes that control the perovskite film's grain size are expected to be substrate-dependent. The average grain size/film thickness aspect ratio of $FA_{0.05}MA_{0.95}PbI_3$ on PEDOT:PSS (Figure 2e) and PTAA (Figure 2f) is 0.63 and 0.57, respectively. On the other hand, most grains in $FA_{0.05}MA_{0.95}PbI_3$ films on CuI were larger than the film thickness, with the average grain size/film thickness aspect ratio of 1.2 for CuI (Figure 2g) and 1.6 for CuI on PTAA (Figure 2h). The increase in average grain size of perovskite over PTAA/CuI HTL, by ~100 nm, compared to CuI alone could be due to the non-wetting nature of PTAA, which can increase CuI crystal size.[23,39,40] These large CuI crystals can mitigate the nucleation of perovskite film that can drive larger grain formation. Surprisingly, unlike previous reports, we did not observe an enhancement in perovskite grain size on PTAA (Figure 2f), perhaps due to the differences in film fabrication methods—one-step antisolvent dripping vs. two-step interdiffusion.[23] It has been widely observed that the large grain size, *i.e.,* a smaller density of grain boundaries, can enhance the V_{OC} due to the elimination of charge trapping and non-radiative recombination. In addition to the increase in grain size, the root mean square (RMS) roughness for the perovskite film deposited on PTAA/CuI was less (8.3 nm) compared to ones on CuI (19.3 nm), PTAA (15.9 nm), and PEDOT:PSS (22.0 nm) (Figure S4). Moreover, using XRD, we observed an enhancement in perovskite (110) peak intensity (Figure S5) when deposited on PTAA/CuI, indicating improved crystallinity compared to other HTLs. As a result, low trap density in PTAA/CuI-based films benefits the device performance.

The energy levels of individual components and their alignment at various hetero-interfaces in the device structures were studied by ultraviolet photoelectron spectroscopy (UPS). **Figure 3**a shows the binding energy region that was used to determine secondary electron cut-off energies (E_{SEC}), and to calculate vacuum level (VL), Fermi level (E_F), and work function. Figure 3b shows the binding energy region that contains the highest occupied molecular orbital (HOMO) or valance band (VB) onsets. The work function of the ITO was 4.85 eV (Figure S6). The energy levels for all HTLs and $FA_{0.05}MA_{0.95}PbI_3$ are summarized in Figure 3c. The work function of PEDOT:PSS was 5.1 eV. The E_F and HOMO of PTAA were 4.6 eV and 5.1 eV, respectively. Note that in contact with materials that can source I^- anions, such as CuI or $FA_{0.05}MA_{0.95}PbI_3$ in our case, iodide anion doping of PTAA could lead to the pinning of E_F as high energy as HOMO, *i.e.,* at 5.1 eV. Such doping of PTAA using copper salts has been observed.[36] The E_F and VB onset for CuI were determined at 5.25 eV and 5.35 eV, respectively. The proximity of E_F to VB indicates that CuI is a highly-doped p-type material (denoted p^{++}-CuI), *i.e.,* possesses high hole carrier density and, hence, electrical conductivity. p-type doping of CuI has been previously attributed to excess I^- anion vacancies.[25,34] High electrical conductivity of CuI ensures a low resistive voltage loss across the interlayer and hence, an efficient charge collection.[25] CuI films deposited on PTAA shifted the E_F towards the VB by 50 meV compared to bare CuI on ITO (Figure S7). Although this difference is below the UPS instrument's resolution limit, such a shift in E_F could occur due to the p-doping of CuI in the presence of excess iodide vacancies. We believe that these excessive vacancies are a result of PTAA doping with iodide anions. The E_F and VB of $FA_{0.05}MA_{0.95}PbI_3$ are 4.9 eV and 5.55 eV, respectively. Herein, we note that the probed depth in the UPS experiment of ~2 nm, as determined by the mean free path for inelastic scattering of electrons, was significantly smaller than the perovskite film thickness of ~350 nm. As a result, the determined energy levels, in particular E_F, describe the properties of top surface of perovskite film. E_F in the bulk or at the hidden interface with substrate can be significantly different due to surface/interface band bending that is determined by the hetero-interfacial Fermi level alignment, magnitudes of interfacial dipoles, and population of surface/interface traps.[41] On the other hand, flattening of surface band bending due to surface photovoltage effect [42] in the UPS experiment under UV illumination and background illumination leads to the measurement of energy levels, which could be characteristic of bulk properties.[43] Figure 3d illustrates the interfacial energy level alignment between p-doped PTAA with a work function of 5.1 eV and $FA_{0.05}MA_{0.95}PbI_3$ with a work function of 4.9 eV. Assuming an ideal interface, *i.e.,* no interfacial dipole or surface traps, such work function difference would lead to the upward interfacial band bending of 0.2 eV. The larger work function of

a p^{++}-CuI of 5.25 eV can lead to an increased band bending of 0.35 eV, facilitating the hole extraction at this interface. Additionally, the p++-CuI electrode can support a larger splitting of quasi-Fermi levels in the device active layer under illumination, leading to larger V_{OC}.

The alignment of energy levels of PEDOT:PSS, PTAA, CuI, and PTAA/CuI at HTL/perovskite interface in PSCs devices can be inferred from the impedance spectroscopy, using the Mott-Schottky analysis.[44,45] We note that application of a depletion layer theory for metal-semiconductor interface with

The static charge distribution, which Mott-Schottky analysis implies, to PSCs should be exercised with caution due to ionic contributions and electrode polarization effects.[46,47] **Figure 4** shows the dependence of C^{-2} on the applied bias (where C is the device capacitance) for two opposite scan directions and a scan rate of 117 mV s^{-1} (identical to DC *J-V* measurements). As follows from variations in scan rates (Figure S8), the curves that were measured in the reverse direction for PTAA- and PTAA/CuI-based devices are independent of a scan rate and nearly coincide with the curve that was measured in the forward direction at the slowest scan rate, hence making Mott-Schottky analysis less prone to hysteresis. As discussed in Ref. [45], positive polarization as a starting point in *C-V* measurements, *i.e.,* reverse scan direction, is likely to remove the non-depletion-related contributions to the capacitance that obstruct determination of a built-in potential (V_{bi}) from Mott-Schottky analysis. Fitting the linear regions of reverse scan curves in Figures 4b and 4c by **Equation (1)**, the V_{bi} values of ~1.24 V and 1.28 V for PTAA- and PTAA/CuI-based devices, respectively, were determined. Both V_{bi} values are slightly smaller than the work function difference between the respective HTL and C_{60}-N/Ag electrode (work function = 3.65 eV, Ref. [20]). A slightly larger V_{bi} for PTAA/CuI-based devices is also in agreement with the larger work function of p^{++}-CuI (5.25 eV) compared to the work function of p-doped PTAA (5.10 eV) and correlates with the larger V_{OC} of CuI- and PTAA/CuI-based devices. The quasi-Fermi level for holes would be pinned at the larger work function of p^{++}-CuI, leading to a larger V_{OC} in these devices.

$$\frac{1}{C^2} = \frac{2}{q\varepsilon_0\varepsilon N_B}(V - V_{bi} - 2kT/q) \quad (1)$$

where q is the elementary charge, ε_0 is the vacuum permittivity, ε is the relative dielectric constant of perovskite material, N_B is either donor or acceptor concentration depending on the conductivity type, V_{bi} is the built-in potential, k is Boltzman's constant, and T is the absolute temperature.

The difference in V_{bi} values for opposite scan directions for PTAA- and PTAA/CuI-based devices, 0.06 V and 0.13 V, respectively, as determined from the Mott-Schottky analysis (ΔV_{bi} in Figure 4(b) and 4(c)) or 0.17 V and 0.06 V, respectively, as estimated for a broader set of scan rates from the difference in the minima of $C^{-2}(V)$ curves (ΔV_{min} in Figure S8) allows to estimate the extent of hysteresis that is associated with each HTL. Note that, while devices with PEDOT:PSS HTL operate with virtually no hysteresis (Figure S2(c), Table S2), the performance of CuI-based HTL devices is highly affected by the scan parameters (Figure 4(d), Figure S2(b), Table S2) and depends on measurement history. Identical to the behavior observed for DC *J-V* curves, the presence of PTAA in a bilayer PTAA/CuI-based devices significantly suppresses the hysteresis in *C-V* curves that devices with single CuI-based HTL demonstrate, making the performance of PTAA- and PTAA/CuI-based devices comparable.

We employed the steady-state photoluminescence (PL) spectroscopy to characterize hole extraction efficiency for different HTLs. A strong emission peak was observed around ~775 nm (Figure S9), consistent with the 1.57 eV bandgap calculated from the Tauc plot (Figure S10). The PTAA/CuI and CuI underlayer quenched the $FA_{0.05}MA_{0.95}PbI_3$ emission, and the quenching was stronger in the case of PTAA/CuI. The smaller PL intensity is associated with less radiative losses. A reduced radiative recombination in bilayer containing devices explains a higher V_{OC} and *FF*.[28,48,49]

We also employed impedance spectroscopy (IS) to investigate the recombination resistance (R_{rec}) in different HTL-based PSCs. The IS data for different HTL containing PSCs (Figure S11) was fit to an equivalent circuit model reported elsewhere.[21,47,50] The R_{rec} for different HTLs are given in Table S3. The PTAA/CuI-containing device has a highest R_{rec}, followed by CuI and PTAA. Meanwhile, PEDOT:PSS-based device has the lowest recombination resistance. Since the perovskite/ETL interface is same for all devices, we ascribe the difference in R_{rec} to the HTL/perovskite interface. This result is consistent with the UPS data, which suggests a better HOMO alignment

Figure 4. Mott-Schottky plot of PSCs containing different HTLs under forward (solid circles) and reverse (open circles) direction. The solid lines are the fits in the respective voltage regions, and dashed lines are a guide. The *C-V* measurements were performed at 10 kHz with a scan rate of 117 mV/s.

of CuI with the HOMO of perovskite (Figure 3c), hence, ensures reduced recombination.

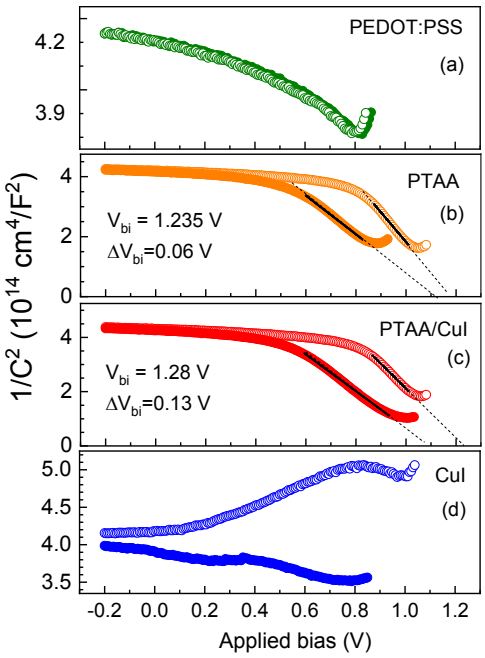

The current output stability of devices with different HTLs was tested by tracking the maximum power point (MPP), as shown in **Figure 5**a. The devices were kept at V_{MP} under AM1.5G light and the resulting current was measured over a period of 200 s. The results indicate that both PTAA (V_{MP} = 0.857 V) and PTAA/CuI (V_{MP} = 0.900 V) HTLs produce more stable output at MPP relative to other HTLs employed. The worst performance was observed in CuI-based devices (V_{MP} = 0.887 V) which showed ~11% decrease in the current within first 200 s. We expect a similar decrease in current during the reverse voltage scan, although the rate of decay could be different. This observation corroborates with the *J-V* scans for CuI-based devices (Figure S1b) which showed significant hysteresis

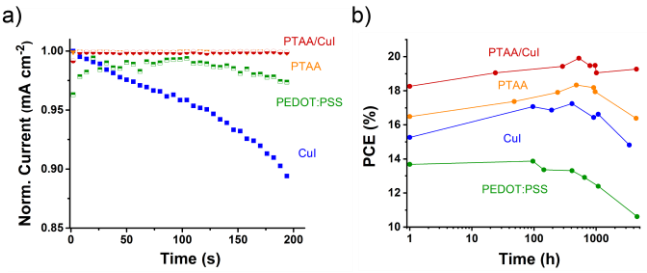

Figure 5. (a) Normalized current-density output of devices employing different HTLs as a function of time under maximum power-point (MPP) tracking test; (b) the long term (> 3000 h) stability test of CuI, PTAA/CuI, PTAA and PEDOT:PSS-based $FA_{0.05}MA_{0.95}PbI_3$ devices stored inside inert N_2-filled glove box under white fluorescent light.

on switching the scan direction. The stable power output of different HTL containing devices at MPP is also given Figure S12.

Long-term stability of devices with CuI, PTAA, PTAA/CuI and PEDOT:PSS HTLs was tested by storing them in inert atmosphere of a glovebox (without encapsulation, under white fluorescent light) for over 3000 h. As shown in Figure 5b, CuI-, PTAA- and PTAA/CuI-based devices show superior stability over PEDOT:PSS-based ones. While a minimal decrease in PCE was observed after 408 h, 480 h and 528 h, respectively, the PCE of PEDOT:PSS-based devices drops significantly only after 144 h of storage. The PTAA/CuI containing devices maintained their stability even after 4500 h (Figure 5b). Since, the only difference between these PSCs is the HTL, these results confirm that the PTAA/CuI bilayer is most effective for suppressing device degradation. Similarly, devices with double layer CuI/PEDOT:PSS as HTL have demonstrated an improved efficiency and stability; however, only when CuI was placed in-between ITO and PEDOT:PSS, removing a corrosive effect of PEDOT:PSS on ITO.[28]

4. Conclusion

In this work, we employed a PTAA/CuI bilayer as an HTL in inverted PSC and showed a significant enhancement of device PCE and long-term stability compared to devices with single PEDOT:PSS, PTAA, or CuI HTLs. These improvements originate from each layer's properties as well as from their interaction in the bilayer HTL. The AFM and XRD results show that the CuI surface facilitates the growth of larger perovskite grains and improves their crystallinity. Using UPS, we determine the energy levels of each component in the device architecture. Combined with the Mott-Schottky analysis of the impedance spectra, we found that the bilayer creates an enhanced upward band bending of 0.35 eV at the CuI/perovskite interface and a large V_{bi} of ~1.28 V throughout the active layer, favoring the charge extraction at both sides. The higher work function of CuI is responsible for higher *Voc* of the devices since the pinning of the quasi-Fermi level for holes under illumination can occur at a deeper level. We believe that the device architecture with bilayer HTLs is a promising route for further improvement of efficiency and stability of perovskite solar cells. Through a deeper understanding of the working mechanisms, which allows for proper design of interfaces, including the energy-level alignment, interfacial engineering could pave the way for further developments of efficient and stable PSCs.

ASSOCIATED CONTENT

Supporting Information

Structure of C_{60}-N, Device parameters, Forward and reverse scan *J-V* curves, Device parameters under forward and reverse scan, EQE profile of multiple PTAA/CuI containing devices, RMS roughness of the perovskite films, XRD pattern for $FA_{0.05}MA_{0.95}PbI_3$ films, UPS spectra of ITO substrates, UPS spectra of CuI film on ITO and PTAA/ITO substrates, Mott-Schottky analysis at different scan rates and directions, PL spectra of $FA_{0.05}MA_{0.95}PbI_3$ films on different HTLs, Tauc plot for $FA_{0.05}MA_{0.95}PbI_3$, Nyquist plots and equivalent circuit fits for different HTL devices, Recombination resistance for different HTL devices, stable power output of devices at MPP.

The Supporting Information is available free of charge on the ACS Publications website.

AUTHOR INFORMATION

Corresponding Author

* D. Venkataraman
E-mail: dv@chem.umass.edu
* Volodimyr V. Duzhko

E-mail: duzhko@mail.pse.umass.edu

Author

Hamza Javaid
ORCID iD: 0000-0002-8845-0676

Author Contributions

All authors have given approval to the final version of the manuscript.

Funding Sources

The work is supported by Army Natick Soldier R D and E Center through contract no. W911QY1820002.

ACKNOWLEDGMENT

We gratefully acknowledge the Laboratory for Electronic Materials and Devices of the Institute for Applied Life Sciences at the University of Massachusetts, Amherst for the device fabrication and characterization facilities. We also thank Prof. Todd Emrick for providing C_{60}-N interlayer.

REFERENCES

(1) Kojima, A.; Teshima, K.; Shirai, Y.; Miyasaka, T. Organometal Halide Perovskites as Visible-Light Sensitizers for Photovoltaic Cells. *J. Am. Chem. Soc.* **2009**, *131*, 6050-6051.

(2) Kim, H.-S.; Lee, C.-R.; Im, J.-H.; Lee, K.-B.; Moehl, T.; Marchioro, A.; Moon, S.-J.; Humphry-Baker, R.; Yum, J.-H.; Moser, J. E.; Grätzel, M.; Park, N.-G. Lead Iodide Perovskite Sensitized All-Solid-State Submicron Thin Film Mesoscopic Solar Cell with Efficiency Exceeding 9%. *Sci. Rep.* **2012**, *2*, 591.

(3) Lee, M. M.; Teuscher, J.; Miyasaka, T.; Murakami, T. N.; Snaith, H. J. Efficient Hybrid Solar Cells Based on Meso-Superstructured Organometal Halide Perovskites. *Science.* **2012**, *338*, 643-647.

(4) NREL. Best Research-Cell Efficiency Chart.

(5) Burschka, J.; Pellet, N.; Moon, S.-J.; Humphry-Baker, R.; Gao, P.; Nazeeruddin, M. K.; Grätzel, M. Sequential Deposition as a Route to High-Performance Perovskite-Sensitized Solar Cells. *Nature* **2013**, *499*, 316–319.

(6) Yang, W. S.; Noh, J. H.; Jeon, N. J.; Kim, Y. C.; Ryu, S.; Seo, J.; Seok, S. Il. High-Performance Photovoltaic Perovskite Layers Fabricated through Intramolecular Exchange. *Science.* **2015**, *348*, 1234 –1237.

(7) Jeon, N. J.; Noh, J. H.; Kim, Y. C.; Yang, W. S.; Ryu, S.; Seok, S. Il. Solvent Engineering for High-Performance Inorganic–Organic Hybrid Perovskite Solar Cells. *Nat. Mater.* **2014**, *13*, 897–903.

(8) Zheng, X.; Chen, B.; Dai, J.; Fang, Y.; Bai, Y.; Lin, Y.; Wei, H.; Zeng, X. C.; Huang, J. Defect Passivation in Hybrid Perovskite Solar Cells Using Quaternary Ammonium Halide Anions and Cations. *Nat. Energy* **2017**, *2*, 17102.

(9) Wu, Y.; Yang, X.; Chen, W.; Yue, Y.; Cai, M.; Xie, F.; Bi, E.; Islam, A.; Han, L. Perovskite Solar Cells with 18.21% Efficiency and Area over 1 cm^2 Fabricated by Heterojunction Engineering. *Nat. Energy* **2016**, *1*, 16148.

(10) Luo, D.; Yang, W.; Wang, Z.; Sadhanala, A.; Hu, Q.; Su, R.; Shivanna, R.; Trindade, G. F.; Watts, J. F.; Xu, Z.; Liu, T.; Chen, K.; Ye, F.; Wu, P.; Zhao, L.; Wu, J.; Tu, Y.; Zhang, Y.; Yang, X.; Zhang, W.; Friend, R. H.; Gong, Q.; Snaith, H. J.; Zhu, R. Enhanced Photovoltage for Inverted Planar Heterojunction Perovskite Solar Cells. *Science.* **2018**, *360*, 1442–1446.

(11) Sha, W. E. I.; Ren, X.; Chen, L.; Choy, W. C. H. The Efficiency Limit of $CH_3NH_3PbI_3$ Perovskite Solar Cells. *Appl. Phys. Lett.* **2015**, *106*, 221104.

(12) Saliba, M.; Matsui, T.; Domanski, K.; Seo, J.-Y.; Ummadisingu, A.; Zakeeruddin, S. M.; Correa-Baena, J.-P.; Tress, W. R.; Abate, A.; Hagfeldt, A.; Grätzel, M. Incorporation of Rubidium Cations into Perovskite Solar Cells Improves Photovoltaic Performance. *Science.* **2016**, *354*, 206–209.

(13) Bi, D.; Yi, C.; Luo, J.; Décoppet, J.-D.; Zhang, F.; Zakeeruddin, S. M.; Li, X.; Hagfeldt, A.; Grätzel, M. Polymer-Templated Nucleation and Crystal Growth of Perovskite Films for Solar Cells with Efficiency Greater than 21%. *Nat. Energy* **2016**, *1*, 16142.

(14) Min, H.; Kim, M.; Lee, S.-U.; Kim, H.; Kim, G.; Choi, K.; Lee, J. H.; Seok, S. Il. Efficient, Stable Solar Cells by Using Inherent Bandgap of α-Phase Formamidinium Lead Iodide. *Science.* **2019**, *366*, 749–753.

(15) Jeng, J.-Y.; Chiang, Y.-F.; Lee, M.-H.; Peng, S.-R.; Guo, T.-F.; Chen, P.; Wen, T.-C. $CH_3NH_3PbI_3$ Perovskite/Fullerene Planar-Heterojunction Hybrid Solar Cells. *Adv. Mater.* **2013**, *25*, 3727–3732.

(16) Docampo, P.; Ball, J. M.; Darwich, M.; Eperon, G. E.; Snaith, H. J. Efficient Organometal Trihalide Perovskite Planar-Heterojunction Solar Cells on Flexible Polymer Substrates. *Nat. Commun.* **2013**, *4*, 2761.

(17) Zhu, R. Inverted Devices Are Catching Up. *Nat. Energy* **2020**, *5*, 123–124.

(18) Zheng, X.; Hou, Y.; Bao, C.; Yin, J.; Yuan, F.; Huang, Z.; Song, K.; Liu, J.; Troughton, J.; Gasparini, N.; Zhou, C.; Lin, Y.; Xue, D.-J.; Chen, B.; Johnston, A. K.; Wei, N.; Hedhili, M. N.; Wei, M.; Alsalloum, A. Y.; Maity, P.; Turedi, B.; Yang, C.; Baran, D.; Anthopoulos, T. D.; Han, Y.; Lu, Z.-H.; Mohammed, O. F.; Gao, F.; Sargent, E. H.; Bakr, O. M. Managing Grains and Interfaces via Ligand Anchoring Enables 22.3%-Efficiency Inverted Perovskite Solar Cells. *Nat. Energy* **2020**, *5*, 131–140.

(19) Heeger, A. J. 25th Anniversary Article: Bulk Heterojunction Solar Cells: Understanding the Mechanism of Operation. *Adv. Mater.* **2014**, *26*, 10–28.

(20) Page, Z. A.; Liu, Y.; Duzhko, V. V; Russell, T. P.; Emrick, T. Fulleropyrrolidine Interlayers: Tailoring Electrodes to Raise Organic Solar Cell Efficiency. *Science.* **2014**, *346*, 441–444.

(21) Bag, M.; Renna, L. A.; Adhikari, R.; Karak, S.; Liu, F.; Lahti, P. M.; Russell, T. P.; Tuominen, M. T.; Venkataraman, D. Kinetics of Ion Transport in Perovskite Active Layers and Its Implications for Active Layer Stability. *J. Am. Chem. Soc.* **2015**, *137*, 13130–13137.

(22) Zuo, C.; Bolink, H. J.; Han, H.; Huang, J.; Cahen, D.; Ding, L. Advances in Perovskite Solar Cells. *Adv. Sci.* **2016**, *3*, 1500324.

(23) Bi, C.; Wang, Q.; Shao, Y.; Yuan, Y.; Xiao, Z.; Huang, J. Non-Wetting Surface-Driven High-Aspect-Ratio Crystalline Grain Growth for Efficient Hybrid Perovskite Solar Cells. *Nat. Commun.* **2015**, *6*, 7747.

(24) Ni, Z.; Bao, C.; Liu, Y.; Jiang, Q.; Wu, W.-Q.; Chen, S.; Dai, X.; Chen, B.; Hartweg, B.; Yu, Z.; Holman, Z.; Huang, J. Resolving Spatial and Energetic Distributions of Trap States in Metal Halide Perovskite Solar Cells. *Science.* **2020**, *367*, 1352–1358.

(25) Christians, J. A.; Fung, R. C. M.; Kamat, P. V. An Inorganic Hole Conductor for Organo-Lead Halide Perovskite Solar Cells. Improved Hole Conductivity with Copper Iodide. *J. Am. Chem. Soc.* **2014**, *136*, 758–764.

(26) Chen, W.-Y.; Deng, L.-L.; Dai, S.-M.; Wang, X.; Tian, C.-B.; Zhan, X.-X.; Xie, S.-Y.; Huang, R.-B.; Zheng, L.-S. Low-Cost Solution-Processed Copper Iodide as an Alternative to PEDOT:PSS Hole Transport Layer for Efficient and Stable Inverted Planar Heterojunction Perovskite Solar Cells. *J. Mater. Chem. A* **2015**, *3*, 19353–19359.

(27) Duzhko, V. V; Dunham, B.; Rosa, S. J.; Cole, M. D.; Paul, A.; Page, Z. A.; Dimitrakopoulos, C.; Emrick, T. N-Doped Zwitterionic Fullerenes as Interlayers in Organic and Perovskite Photovoltaic Devices. *ACS Energy Lett.* **2017**, *2*, 957–963.

(28) Hu, W.-D.; Dall'Agnese, C.; Wang, X.-F.; Chen, G.; Li, M.-Z.; Song, J.-X.; Wei, Y.-J.; Miyasaka, T. Copper Iodide-PEDOT:PSS Double Hole Transport Layers for Improved Efficiency and Stability in Perovskite Solar Cells. *J. Photochem. Photobiol. A Chem.* **2018**, *357*, 36–40.

(29) Peng, H.; Sun, W.; Li, Y.; Ye, S.; Rao, H.; Yan, W.; Zhou, H.; Bian, Z.; Huang, C. Solution Processed Inorganic V2Oxas Interfacial Function Materials for Inverted Planar-Heterojunction Perovskite Solar Cells with Enhanced Efficiency. *Nano Res.* **2016**, *9*, 2960–2971.

(30) Pelicano, C. M.; Yanagi, H. Effect of Rubrene:P3HT Bilayer on Photovoltaic Performance of Perovskite Solar Cells with Electrodeposited ZnO Nanorods. *J. Energy Chem.* **2018**, *27*, 455–462.

(31) Mali, S. S.; Patil, J. V; Arandiyan, H.; Luque, R.; Hong, C. K. Editors' Choice—Stability of Unstable Perovskites: Recent Strategies for Making Stable Perovskite Solar Cells. *ECS J. Solid State Sci. Technol.* **2019**, *8*, 111–117.

(32) Li, R.; Wang, P.; Chen, B.; Cui, X.; Ding, Y.; Li, Y.; Zhang, D.; Zhao, Y.; Zhang, X. NiOx/Spiro Hole Transport Bilayers for Stable Perovskite Solar Cells with Efficiency Exceeding 21%. *ACS Energy Lett.* **2020**, *5*, 79–86.

(33) Zhang, W.; Wan, L.; Fu, S.; Li, X.; Fang, J. Reducing Energy Loss and Stabilising the Perovskite/Poly (3-Hexylthiophene) Interface through a Polyelectrolyte Interlayer. *J. Mater. Chem. A* **2020**, *8*, 6546–6554.

(34) Samu, G. F.; Scheidt, R. A.; Balog, Á.; Janáky, C.; Kamat, P. V. Tuning the Excited-State Dynamics of CuI Films with Electrochemical Bias. *ACS Energy Lett.* **2019**, *4*, 702–708.

(35) Sepalage, G. A.; Meyer, S.; Pascoe, A.; Scully, A. D.; Huang, F.; Bach, U.; Cheng, Y.-B.; Spiccia, L. Copper(I) Iodide as Hole-Conductor in Planar Perovskite Solar Cells: Probing the Origin of J–V Hysteresis. *Adv. Funct. Mater.* **2015**, *25*, 5650–5661.

(36) Liu, Y.; Liu, Z.; Lee, E.-C. High-Performance Inverted Perovskite Solar Cells Using Doped Poly(Triarylamine) as the Hole Transport Layer. *ACS Appl. Energy Mater.* **2019**, *2*, 1932–1942.

(37) Louboutin, J. P.; Beniere, F. Doping Mechanism of a Conducting Polymer: Iodine-Doped Polyacetylene. *J. Phys. Chem. Solids* **1982**, *43*, 233–241.

(38) Boyle, C. J.; Upadhyaya, M.; Wang, P.; Renna, L. A.; Lu-Díaz, M.; Pyo Jeong, S.; Hight-Huf, N.; Korugic-Karasz, L.; Barnes, M. D.; Aksamija, Z.; Venkataraman, D. Tuning Charge Transport Dynamics via Clustering of Doping in Organic Semiconductor Thin Films. *Nat. Commun.* **2019**, *10*, 2827.

(39) Yao, Y.; Hsu, W.; Dagenais, M. High-Efficiency Perovskite Solar Cell Based on Sequential Doping of PTAA. *IEEE J. Photovoltaics* **2019**, *9*, 1025–1030.

(40) Lee, H. K. H.; Barbé, J.; Meroni, S. M. P.; Du, T.; Lin, C.-T.; Pockett, A.; Troughton, J.; Jain, S. M.; De Rossi, F.; Baker, J.; Carnie, M. J.; McLachlan, M. A.; Watson, T. M.; Durrant, J. R.; Tsoi, W. C. Outstanding Indoor Performance of Perovskite Photovoltaic Cells - Effect of Device Architectures and Interlayers. *Sol. RRL* **2019**, *3*, 1800207.

(41) Schulz, P.; Cahen, D.; Kahn, A. Halide Perovskites: Is It All about the Interfaces? *Chem. Rev.* **2019**, *119*, 3349–3417.

(42) Duzhko, V.; Koch, F.; Dittrich, T. Transient Photovoltage and Dielectric Relaxation Time in Porous Silicon. *J. Appl. Phys.* **2002**, *91*, 9432–9434.

(43) Zu, F.; Amsalem, P.; Ralaiarisoa, M.; Schultz, T.; Schlesinger, R.; Koch, N. Surface State Density Determines the Energy Level Alignment at Hybrid Perovskite/Electron Acceptors Interfaces. *ACS Appl. Mater. Interfaces* **2017**, *9*, 41546–41552.

(44) Sze, S. M.; Ng, K. K. *Physics of Semiconductor Devices*; John wiley & sons, 2006.

(45) Karak, S.; Lim, J. A.; Ferdous, S.; Duzhko, V. V; Briseno, A. L. Photovoltaic Effect at the Schottky Interface with Organic Single Crystal Rubrene. *Adv. Funct. Mater.* **2014**, *24*, 1039–1046.

(46) Almora, O.; Aranda, C.; Mas-Marzá, E.; Garcia-Belmonte, G. On Mott-Schottky Analysis Interpretation of Capacitance Measurements in Organometal Perovskite Solar Cells. *Appl. Phys. Lett.* **2016**, *109*, 173903.

(47) Smith, E. C.; Ellis, C. L. C.; Javaid, H.; Renna, L. A.; Liu, Y.; Russell, T. P.; Bag, M.; Venkataraman, D. Interplay Between Ion Transport, Applied Bias and Degradation under Illumination in Hybrid Perovskite p-i-n Devices. *J. Phys. Chem. C* **2018**, *122*, 13986–13994.

(48) Yang, G.; Wang, C.; Lei, H.; Zheng, X.; Qin, P.; Xiong, L.; Zhao, X.; Yan, Y.; Fang, G. Interface Engineering in Planar Perovskite Solar Cells: Energy Level Alignment, Perovskite Morphology Control and High Performance Achievement. *J. Mater. Chem. A* **2017**, *5*, 1658–1666.

(49) Zhou, Z.; Li, X.; Cai, M.; Xie, F.; Wu, Y.; Lan, Z.; Yang, X.; Qiang, Y.; Islam, A.; Han, L. Stable Inverted Planar Perovskite Solar Cells with Low-Temperature-Processed Hole-Transport Bilayer. *Adv. Energy Mater.* **2017**, *7*, 1700763.

(50) Liu, Y.; Renna, L. A.; Thompson, H. B.; Page, Z. A.; Emrick, T.; Barnes, M. D.; Bag, M.; Venkataraman, D.; Russell, T. P. Role of Ionic Functional Groups on Ion Transport at Perovskite Interfaces. *Adv. Energy Mater.* **2017**, *7*, 13.

(51) Endres, J.; Kulbak, M.; Zhao, L.; Rand, B. P.; Cahen, D.; Hodes, G.; Kahn, A. Electronic Structure of the CsPbBr3/Polytriarylamine (PTAA) System. *J. Appl. Phys.* **2017**, *121*, 35304.

(52) Sirimanne, P. M.; Rusop, M.; Shirata, T.; Soga, T.; Jimbo, T. Characterization of CuI Thin Films Prepared by Different Techniques. *Mater. Chem. Phys.* **2003**, *80*, 461–465.

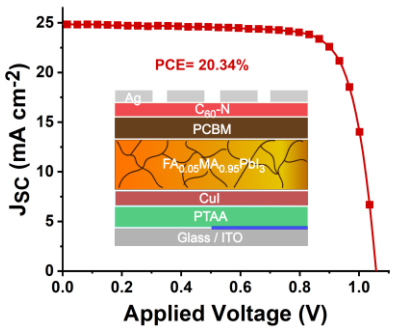
PCE= 20.34%
Ag
C60-N
PCBM
FA0.05MA0.95PbI3
CuI
PTAA
Glass / ITO
Jsc (mA cm-2)
Applied Voltage (V)
0
5
10
15
20
25
0.0
0.2
0.4
0.6
0.8
1.0